ELSEVIER

Ni and O co-modified MoS$_2$ as universal SERS substrate for the detection of different kinds of substances

Rui Su [a,b,c], Shuo Yang [d], Donglai Han [e], Mingyue Hu [a], Yang Liu [a,f], Jinghai Yang [a], Ming Gao [a,*]

[a] Key Laboratory of Functional Materials Physics and Chemistry of the Ministry of Education, Jilin Normal University, Changchun 130103, PR China
[b] University of Chinese Academy of Sciences, Beijing 100049, PR China
[c] Changchun Institute of Optics, Fine Mechanics and Physics, Chinese Academy of Sciences, Changchun 130033, PR China
[d] College of Science, Changchun University, Changchun 130022, PR China
[e] School of Materials Science and Engineering, Changchun University of Science and Technology, Changchun 130022, PR China
[f] Key Laboratory of Novel Materials for Sensor of Zhejiang Province, Hangzhou Dianzi University, Hangzhou 310012, PR China

HIGHLIGHTS

- The ultra-high SERS activity of MoS$_2$ is realized by Ni and O co-modification.
- The 1NMS$_{250-3h}$ substrate has a high EF value of 7.73×10^6.
- The 1NMS$_{250-3h}$ substrate can realize rapid detection of various molecules.
- Synergistic SERS enhancement mechanism for 1NMS$_{250-3h}$.

GRAPHICAL ABSTRACT

Ni and O co-modified MoS$_2$ as SERS substrate to detect harmful substances, and its enhanced effect came from the charge transfer effect and interface dipole–dipole interaction between substrate and molecules. It doesn't depend on molecular resonance. Thus, it can realize the rapid detection of different kinds of substances.
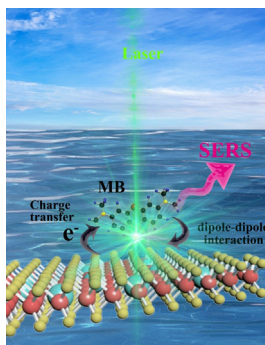
ARTICLE INFO

ABSTRACT

Surface-enhanced Raman scattering (SERS) has attracted extensive attention as an ultrasensitive detection method. However, the poor biocompatibility and expensive synthesis cost of noble metal SERS substrates have become non-negligible factors that limit the development of SERS technology. Metal chalcogenide semiconductors as an alternative to noble metal SERS substrates can avoid these disadvantages, but the enhancement effect is lower than that of noble metal substrates. Here, we report a method to co-modify MoS$_2$ by Ni and O, which improves the carrier concentration and mobility of MoS$_2$. The SERS effect of the modified MoS$_2$ is comparable to that of noble metals. We found that the improved SERS performance of MoS$_2$ can be attributed to the following two factors: strong interfacial dipole–dipole interaction and efficient charge transfer effect. During the doping process, the incorporation of Ni and O enhances the polarity and carrier concentration of MoS$_2$, enhances the interfacial interaction of MoS$_2$, and provides a basis for charge transfer. During the annealing process, the introduction of O atoms into the S defects reduces the internal defects of doped MoS$_2$, improves the carrier mobility, and promotes the efficient charge transfer effect of MoS$_2$. The final modified MoS$_2$ as a SERS substrate realizes low-

---

* Corresponding author at: Key Laboratory of Functional Materials Physics and Chemistry of the Ministry of Education, and National Demonstration Centre for Experimental Physics Education, Jilin Normal University, Siping 136000, PR China.

E-mail address: gaomingphy@126.com (M. Gao).

concentration detection of bilirubin, cytochrome *C*, and trichlorfon. This provides promising guidance for the practical inspection of metal chalcogenide semiconductor substrates.

1. Introduction:

As an ultrasensitive spectroscopic analysis technique, SERS has been widely studied in biological, medical and other fields [1,2]. So far, SERS technology has achieved high-sensitivity detection on noble metal substrates [3]. However, the poor stability and bio-compatibility of noble metals hinder their application in the field of SERS [4]. Thus, the development of semiconductor materials with high cost performance, abundant earth resources and excellent optoelectronic properties has become one of the important tasks at present, in order to replace the noble metal materials [5–9]. Earth-abundant metal-chalcogenide semiconductors offer promise in the fields of photo/electrocatalysis and high-performance devices, due to their excellent carrier mobility and tunable band gap structure [10–12]. And metal-chalcogenide semiconductor materials have also shown great strength in the field of SERS due to their excellent stability and biocompatibility, as well as unique optical properties [13,14]. A recently reported chemical vapor deposition (CVD) method can synthesize metal-chalcogenide semiconductors with excellent optoelectronic properties [15,16]. However, due to the complex process and low yield of this method, mass production of metal-chalcogenide semiconductors still faces insurmountable challenges [17,18]. Hydrothermal method has the advantages of simple synthesis process and high yield, and has become one of the commonly used methods for synthesizing metal-chalcogenide semiconductors [19,20].

Different from the electromagnetic mechanism (EM) of the noble metal materials, the SERS effect of metal-chalcogenide semiconductor materials mainly comes from chemical mechanism (CM), including charge transfer (CT) effect and molecular resonance effect [2]. However, the molecular resonance effect has very strict requirements on the band gap structure of molecules and laser energy, and it is usually difficult to realize the molecular resonance effect [21]. Therefore, the CT effect becomes the main factor affecting the SERS effect of metal-chalcogenide semiconductors. The high charge transport capacity of metal-chalcogenide semiconductor can achieve high charge transfer efficiency. Hence, improving the charge transport ability of metal-chalcogenide semiconductors may be of great significance to improve its SERS effect.

However, due to the low intrinsic semiconductor carrier concentration and the generation of numerous defects during the hydrothermal synthesis, the optoelectronic properties of the synthesized samples are seriously affected. Doping can replace atoms in a material, thereby increasing the carrier density and electrical conductivity of the material. This helps to enhance the charge transfer process at the material interface, providing a promising scheme for tuning the optoelectronic properties of the material [22,23]. Annealing can effectively eliminate defect states in metal-chalcogenide semiconductors and improve the transport properties and quantum efficiency in semiconductors [24]. This is due to the O_2 adsorbed on the defect structure of the metal-chalcogenide semiconductor can be separated into O atoms, one at the defect and the other combined with the adjacent S-series elements to form a group. The O at the defect has the same valence as the anion in the metal-chalcogenide semiconductor, thus facilitates the elimination of the defect state [25].

Here, we use Ni and O co-modify MoS_2 to enhance the SERS effect of MoS_2. In our previous work, the optimal Ni-doping MoS_2

(1NMS NFs) substrate has been shown to have the strongest SERS effect [26]. We further annealed the 1NMS NFs to reduce defects and improve carrier transport efficiency. The optimized MoS_2 NFs exhibited a higher level of SERS effect, and the Raman signal of methylene blue (MB) was greatly enhanced with an enhancement factor of 7.73×10^6. Density functional theory (DFT) calculations show that the ultrasensitive SERS effect of the optimized MoS_2 NFs mainly comes from their strong adsorption energy and efficient charge transfer ability. This is in good agreement with the conclusions drawn from our experimental results, and also demonstrates that this method can effectively enhance the optoelectronic properties of hydrothermally synthesized metal chalcogenide semiconductors. Finally, the low-concentration detection of bilirubin, cytochrome *C* and trichlorfon was realized using this substrate. This work provides a simple method for low-cost detection of hazardous substances.

2. Results and discussion:

2.1. Structure and morphology of modified MoS_2 NFs

Fig. 1 shows the synthesis process of annealed 1NMS (1NMS_temperature-time) samples under different conditions (the experimental detail part refer to supporting information). First, MoS_2 with different Ni-doped amounts were synthesized and their SERS performance were evaluated in our previous work [26]. Then select 1NMS with the best SERS performance for further annealing under different conditions. Details of the experimental methods, please refer to the "Experimental" in supporting information. Fig. 2(a)-(f) show the SEM images of 1NMS NFs annealed temperature range of 0–400 °C in air for 3 h. With annealing temperature exceed 350 °C, the morphology of the samples changed from flower to massive blocky structure. To explore the composition of the samples, the samples were analyzed by XRD and Raman spectra (Fig. 2(g)-(h)). The XRD patterns of the samples annealed at 200, 250 and 300 °C can easily assign the three peaks around $2\theta = 14.4°$, $32.8°$ and $58.6°$ to the (002), (100) and (110) reflections of 2H-MoS_2 (JCPDS 37-1492) [27]. In the Raman spectra of the annealed samples at 200, 250 and 300 ℃, the unique vibration bands of E_{2g}^1 (in-plane) and A_{1g} (out-of-plane) of MoS_2 NFs can also be observed around 381 and 407 cm^{-1} [28]. In addition, as the annealing temperature of MoS_2 NFs under 300 °C, no impurity peaks other than MoS_2 NFs were detected in the XRD and Raman spectra. This shows that no impurities other than MoS_2 NFs are formed after annealing. However, when the annealing temperature reached 350 °C, the XRD and Raman spectra of the sample changed significantly. In the XRD pattern, the peaks around $2\theta = 12.7°$, $23.3°$, $25.6°$, $27.3°$, $38.9°$ and $49.2°$ are related to the (020), (110), (040), (021), (081) and (002) reflections of MoO_3 (JCPDS 05–0508) [5,29]. At the same time, in the Raman spectrum, except for the two unique vibration modes of MoS_2 NFs at 381 and 407 cm^{-1}, the new Raman peaks are all attributed to MoO_3 [30,31]. When the annealing temperature reaches 400 °C, the sample has better crystallinity through XRD patterns and Raman patterns. And the characteristic peaks belonging to MoS_2 NFs have all disappeared, which shows that MoS_2 NFs has been completely transformed into MoO_3 at high temperature.

The SERS behavior of the annealed and unannealed samples were investigated using Raman. The SERS performance of the
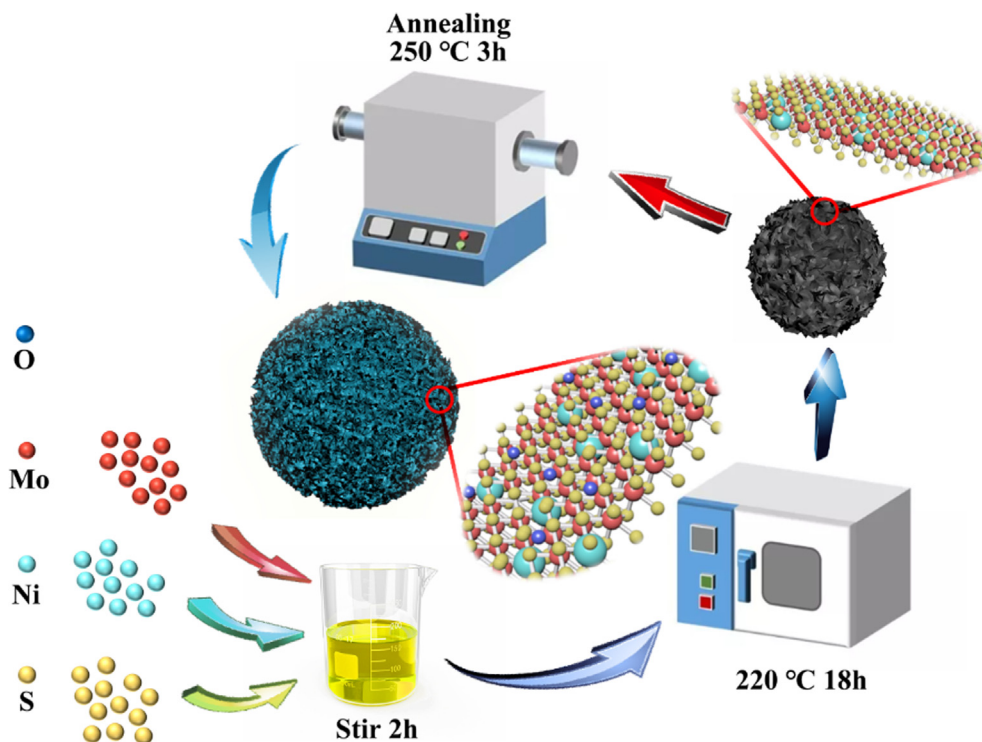
Fig. 1. Schematic diagram of 1NMS$_{250\text{-}3h}$ NFs synthesis.

annealed samples was examined using 10^{-3} M MB as the probe molecule. As shown in Fig. 2(i), when the annealing temperature is 250 °C, the SERS performance is the best. The enhancement factor (EF) can reach 7.73×10^6 (refer to the support information Note 1), which is 20 times that of the unannealed sample (3.56×10^5) and two order of magnitude higher than that of MoS$_2$ (5.537×10^4). MB molecules show significant enhancement at 597, 678, 774, 1397 and 1625 cm^{-1} (the distribution of the vibrational modes of the molecules in Table S1) [32]. Additionally, the XPS of the samples were analyzed. As shown in Fig. 3(a) and Fig. S1(a)-(d), the peaks at 229.3 eV and 232.3 eV are attributed to Mo^{4+} 3d$_{5/2}$ and Mo^{4+} 3d$_{3/2}$ core levels, and the peaks at 233.1 eV and 236.1 eV are attributed to Mo^{6+} 3d$_{5/2}$ and Mo^{6+} 3d$_{3/2}$ core levels [33,34]. With the increase of annealing temperature, Mo^{4+} gradually decreased and Mo^{6+} gradually increased in the sample. This indicates that during the annealing process, Mo^{4+} is partially oxidized to Mo^{6+}, and forming a Mo-O bond [5,35]. Fig. 3(b) and Fig. S1(e)-(h) show the XPS spectra of O 1s core levels of different samples [5]. The deconvolution of the O 1s spectra shows four oxygen-related peaks from different sources. The O 1 s peak at 530.8 eV is attributed to the binding energy of oxygen in the transition metal oxide lattice, which further confirms the formation of Mo-O bonds in the lattice. The peak at 531.8 eV binding energy is related to the oxygen deficient regions. The peak at 532.6 eV is attributed to water adsorbed by the material. The peak at 533.4 eV is bound oxygen on the material surface [5,36]. The change of oxygen correlation peak is related to the change of oxygen concentration. The oxygen concentration of the sample is measured by XPS and listed in Table S2. According to the XPS spectra of Mo 3d and O 1 s core levels of different samples, when the annealing temperature is below 300 °C, the content of Mo^{6+} and the oxygen concentration increase slightly. When the annealing temperature reaches 350 °C or higher, the Mo^{6+} content and oxygen concentration increase significantly, which indicates that materials are oxidized to MoO$_3$. When the annealing temperature reaches 400 °C, the material has been completely oxidized to

MoO$_3$ [37]. This is the same conclusion as XRD and Raman. The 1NMS NFs annealed at 200, 250 and 300 °C all have a small amount of oxygen incorporation. According to previous reports, even a small amount of oxygen incorporation can greatly improve the SERS performance of MoS$_2$ NFs [5]. However, the SERS performance of annealing at 300 °C were not the best. This may be due to the high annealing temperature resulting in more defects, thereby reducing its SERS performance [4]. Fig. 3(c) and 3(d) respectively depict the linear sweep voltammetry (LSV) diagram and electrochemical impedance spectroscopy (EIS) of 1NMS NFs at different annealing temperatures. 1NMS NFs annealed at 250 °C has a smaller charge transfer resistance and a higher current density, which is conducive to charge transfer between substrates and molecules [38,39]. Similarly, the defect structure of the material is largely dependent on the annealing time of the material. According to the results of XRD and Raman, although the annealing time is different, it is not also observed that other impurity peaks appear (Figure S2). But from the XPS spectrum of Mo 3d and O 1s core energy level (Figure S3), the oxygen content gradually increases with time. MoO$_3$ was not observed in the XRD, Raman and SEM spectra (Figure S2 and S4). This indicates that MoO$_3$ cannot be formed at 250 °C, and all oxygen elements doped into the 1NMS lattice. The SERS activities of 1NMS NFs substrates annealed at different times were also evaluated. Figure S5 shows that the SERS performance decreases after annealing for more than 3 h. According to the test results of electrochemical methods such as LSV and EIS (Figure S6), when the annealing time exceeds 3 h, the current density of the material decreases and the charge transfer resistance increases. This is due to the prolonged exposure of 1NMS NFs to air, which makes excess Oxygen atoms incorporated into the lattice of 1NMS NFs. The lattice of 1NMS NFs is distorted to different degrees, which reduces the carrier transport ability in the substrate [40]. Therefore, controlling the carrier transport ability of the substrate by adjusting the annealing time and temperature is very important to improve the SERS performance of substrates.
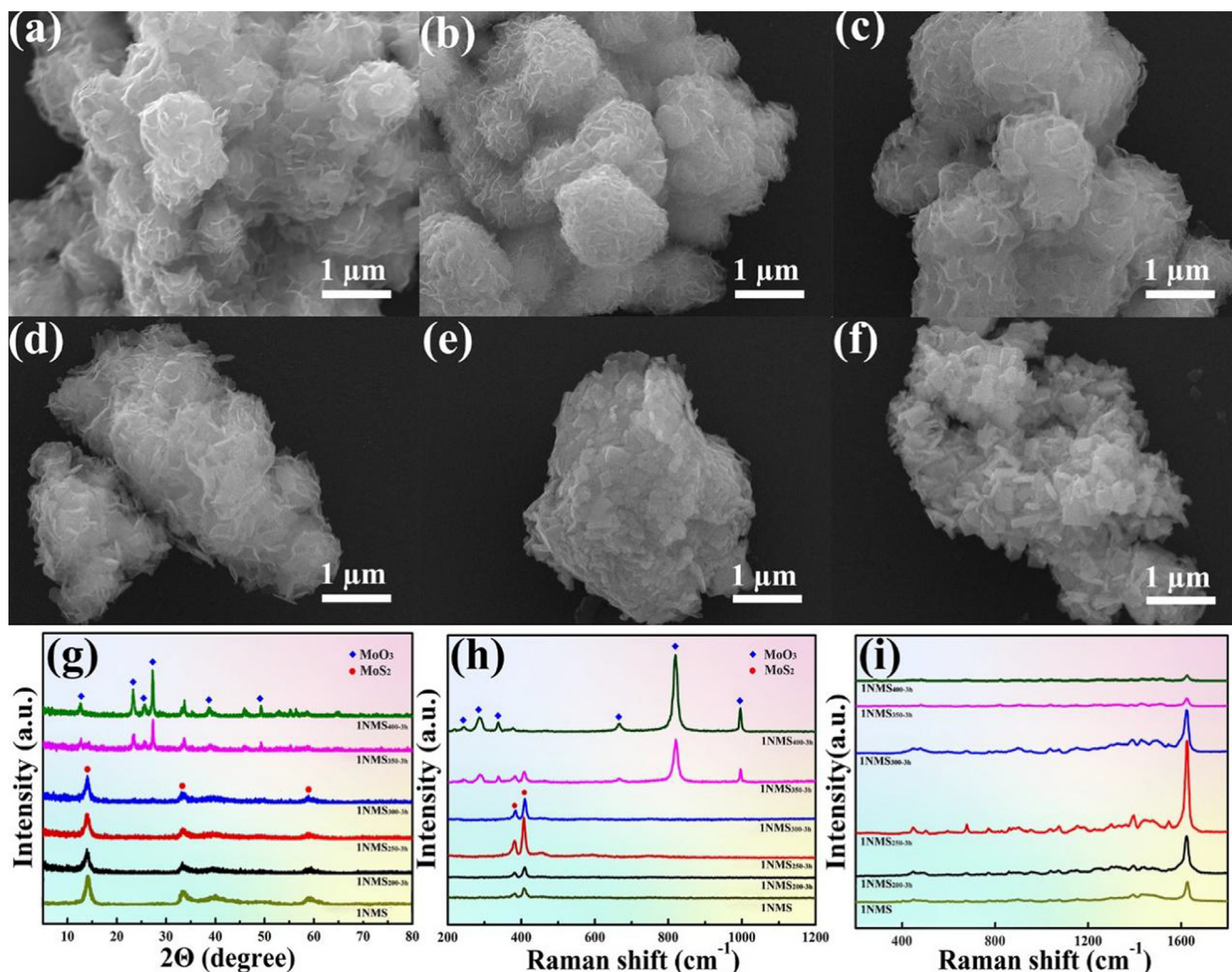
Fig. 2. SEM images of 1NMS annealing at (a) 0 °C, (b) 200 °C, (c) 250 °C, (d) 300 °C, (e) 350 °C and (f) 400 °C at 3 h, respectively. (g) XRD and (h) Raman spectra of 1NMS NFs samples obtained at different annealing temperatures. (i) SERS performance of MB (1×10^{-3} M) at 514 nm collected on six substrates with different annealing temperatures at 3 h.

2.2. Sensitivity, uniformity and stability of 1NMS$_{250-3h}$ NFs substrate

Subsequently, MB was used to evaluate the SERS performance of MoS$_2$, 1NMS and 1NMS$_{250-3h}$ NFs. As shown in Fig. 4(a), the 1NMS$_{250-3h}$ NFs substrate has the highest SERS sensitivity, and its enhancement of MB molecules is much higher than the other two substrates. In addition, we also tested the dyes R6G and RhB (their vibrational mode distributions are shown in Table S3 and Table S4) [41,42], the Raman signal on the 1NMS$_{250-3h}$ NFs substrate is much higher than the other two substrates (Fig. S7(a)-(b)). Meanwhile, the Raman signal can still be observed on the 1NMS$_{250-3h}$ NFs substrate, even if the concentration of the MB is as low as 10^{-9} M (Fig. 4(b) and Fig. S7(c)-(d)). In addition, the 1NMS$_{250-3h}$ NFs substrate also showed good uniformity. On the 1NMS$_{250-3h}$ NFs substrate, 20 points were randomly selected to detect the Raman signal of the MB molecule (Fig. 4(d)), and the relative standard deviation (RSD) was calculated to be 9.3 % (Figure S8). To examine the stability of the 1NMS$_{250-3h}$ NFs, the 1NMS$_{250-3h}$ NFs were stored in the air for 1 month, 2 months, and 3 months. Then the SERS measurement was performed on it (Fig. 4(e)). The Raman peak intensity of MB at 1625 cm^{-1} is decreased by 23.6 % on the substrate stored for 3 months, but the Raman signal could still be clearly observed. The results show that the 1NMS$_{250-3h}$ NFs sample can be stable for at least 3 months.

In order to verify the efficiency of the 1NMS$_{250-3h}$ NFs substrate in actual detection, the detection concentration of MB in water is 1×10^{-3} to 1×10^{-7} M. Fig. 4(f) and Fig. S8(b)–(c) are the SERS spectra of MB in the concentration range. Concentration-dependent average intensity of 3 measurements of the peaks at 1625 cm^{-1} are given in Fig. S8(d). The SERS signals in the 1625 cm^{-1} Raman modes are found to fit the power law dependence of the concentration x$^\alpha$ with α = 2.96 ± 0.10. From this calibration curve, we can estimate the amount of MB.

2.3. SERS enhancement mechanism of 1NMS$_{250-3h}$ NFs

Next, the reasons for excellent SERS sensitivity of 1NMS$_{250-3h}$ NFs were analyzed. According to the unified expression of SERS given by Lombardi et al.:

$$R_{mol-CT}(\omega) = \frac{[(\mu_{mol}^{\alpha} E^{\alpha})(\mu_{CT}^{\beta} E^{\beta}) h_{mol-CT} \langle i|Q_K|f \rangle]}{[(\varepsilon_1(\omega) + 2\varepsilon_0)^2 + \chi \varepsilon_2^2][(\omega_{CT}^2 - \omega^2) + \gamma_{CT}^2][(\omega_{mol}^2 - \omega^2) + \gamma_{mol}^2]}$$

The denominator of the expression contains the product of three resonances, namely plasmon resonance, charge transfer resonance, and molecular resonance [43]. Therefore, we analyze the SERS enhancement mechanism of 1NMS$_{250-3h}$ NFs through the above three aspects. First of all, through calculation, the surface
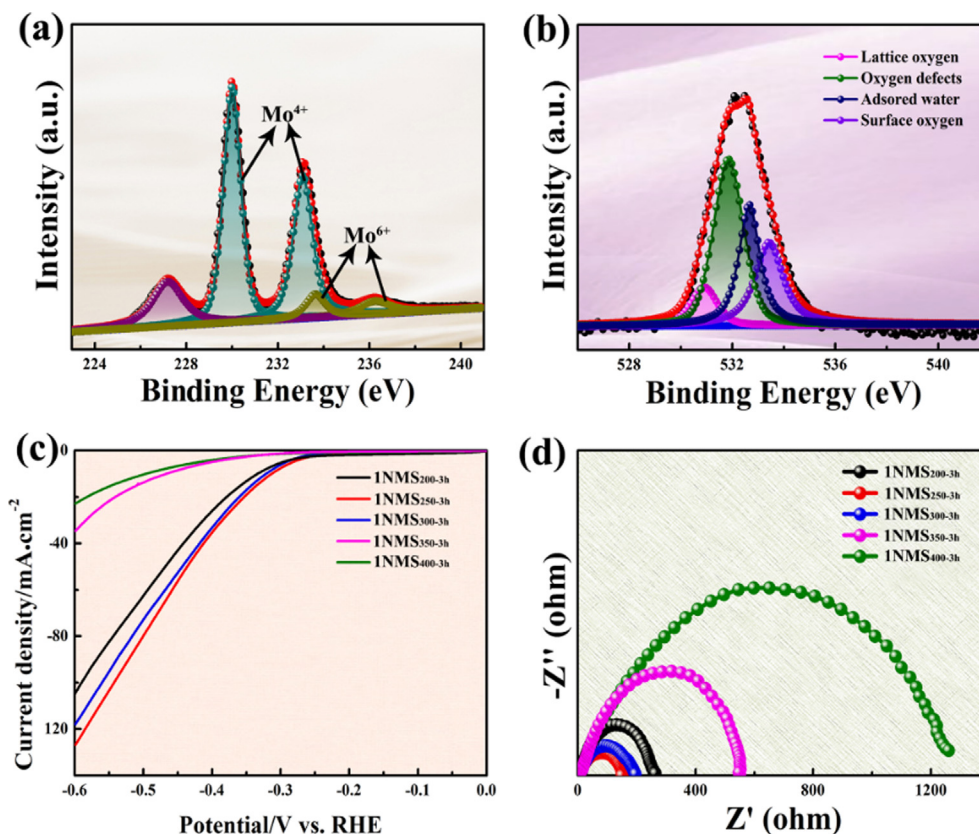
Fig. 3. XPS spectra of 1NMS$_{250-3h}$ NFs: (a) Mo 3d spectrum and (b) O 1s spectrum. (c) LSV curves of 1NMS NFs annealed at different temperatures. (d) Nyquist plots of 1NMS NFs annealed at different temperatures.
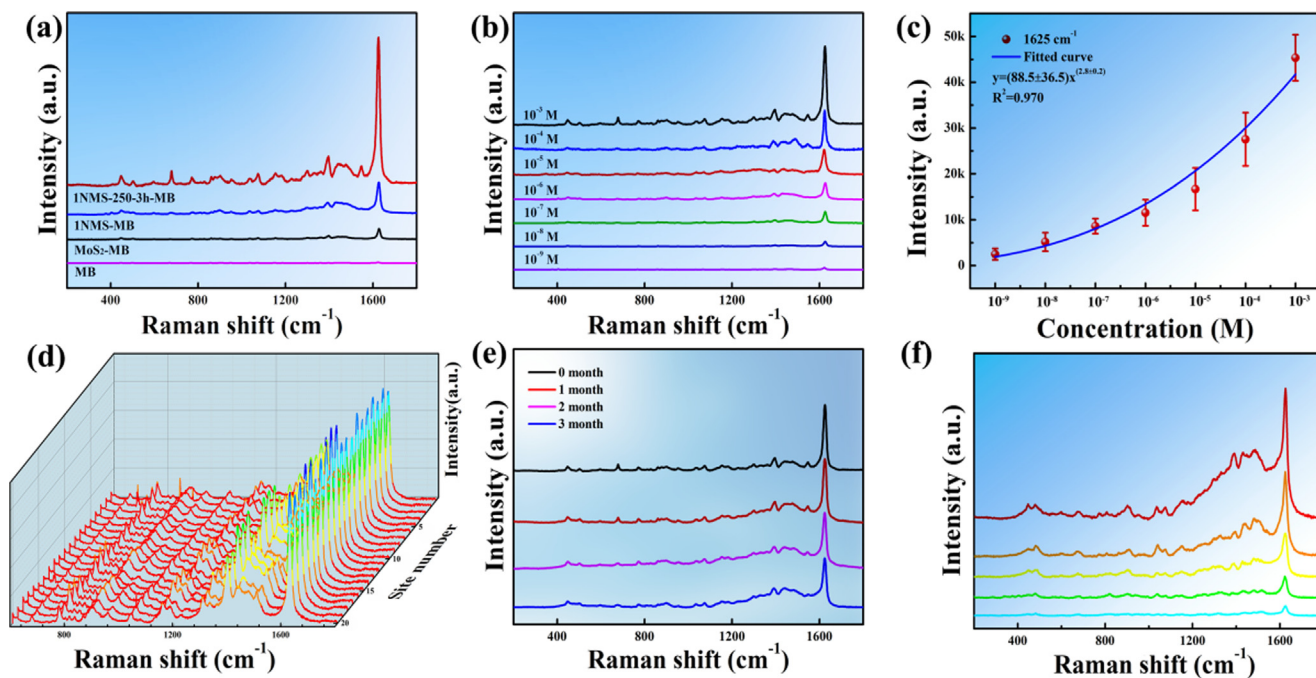

Fig. 4. (a) SERS performance of MB (1×10^{-3} M) at 514 nm collected on 1NMS$_{250-3h}$ NFs, 1NMS NFs, MoS$_2$ NFs and the blank sample collected on glass slide. (b) Raman spectra of MB at concentrations ranging from 10^{-3} to 10^{-9} M collected on 1NMS$_{250-3h}$ NFs. (c) The diagram depicting concentration vs intensity plot of 1625 cm^{-1} modes of MB. (d) Raman spectra MB signal (1×10^{-3} M) obtained on 1NMS$_{250-3h}$ NFs based on the measurements from 100 random spots. (e) SERS spectra of MB tested with 1NMS$_{250-3h}$ NFs s of stored different times. (f) Raman spectra of MB in the real domestic water at concentrations ranging from 10^{-3} to 10^{-7} M collected on 1NMS$_{250-3h}$ NFs.

plasmon resonance (SPR) wavelength λ_p of $1NMS_{250-3h}$ NFs is 6650 nm, which is located in the far-infrared band (support information experiment part 1.6). And according to the UV absorption spectrum (Fig. 5(a)), MoS_2, 1NMS and $1NMS_{250-3h}$ NFs exhibit weak SPR effects in the visible light range. This shows that the contribution of EM to the SERS sensitivity of the substrate can be ignored, and its excellent SERS sensitivity mainly comes from CM. Next, the MB deposited on different substrates were tested under 633 nm laser. Although the energy of 633 nm laser may be better matched with the band gap of MB. However, the Raman signal of MB on different substrates still has a large change (Figure S9), which indicates that molecular resonance is not the main reason for such large differences in SERS sensitivity. Therefore, the charge transfer is the main factor for the high SERS sensitivity of $1NMS_{250-3h}$ NFs.

To understand the reasons for the excellent SERS sensitivity of $1NMS_{250-3h}$ NFs, we investigated from the following two aspects: (1) The interaction between substrates and molecules. (2) Analysis of the basic properties and electronic structure of the substrate. First, the adsorption capacity of MoS_2, 1NMS and $1NMS_{250-3h}$ NFs was tested (Fig. 5(b)). According to the measurement results of MB adsorption differences among the three substrates, the $1NMS_{250-3h}$ NFs substrate has better adsorption capacity. In addition, in Fig. 5(c), the absorption spectrum of the mixture of $1NMS_{250-3h}$ NFs and MB changed most obviously at 615 nm. This indicated that the surface interaction between $1NMS_{250-3h}$ NFs and MB molecules was stronger [4]. This may be due to the formation of localized dangling bonds (Mo—S—O and S—O) on the surface of 1NMS NFs during the annealing process, which enhances the interfacial dipole–dipole interaction between substrates and molecules [36]. In the FTIR (Fig. 5(d)), $1NMS_{250-3h}$ NFs have the most obvious absorptions at 1398 cm^{-1} and 1610 cm^{-1}. This further demonstrated that stronger interactions occurred between substrates and MB molecules [44]. According to the above analysis, $1NMS_{250-3h}$ NFs has stronger adsorption capacity and stronger surface interaction. This is beneficial to the improvement of substrate SERS sensitivity. At the same time, it also provides a basis for better charge transfer between substrates and molecules.

Next, the carrier concentrations of MoS_2, 1NMS and $1NMS_{250-3h}$ NFs were obtained by Hall test (Table S5 and Figure S10). The carrier concentration of 1NMS NFs (1.35×10^{17} /cm^3) and $1NMS_{250-3h}$ NFs (2.91×10^{18} /cm^3) is higher than that of MoS_2 NFs (1.26×10^{16} /cm^3). Among them, Ni doping is the main reason for the increase in the carrier concentration of 1NMS NFs. The high carrier concentration of $1NMS_{250-3h}$ NFs comes from Ni doping and O incorporation during annealing. The same result was obtained by the electrochemical Mott-Schottky diagram (see the supporting information 1.7). In addition, according to the results of the Hall test, $1NMS_{250-3h}$ NFs had the highest mobility and 1NMS NFs had the lowest mobility. (Table S6). We believe that this is related to material defects. According to the results of HRTEM (Figure S11), a large number of defects were present in 1NMS NFs, which resulted in the lowest mobility of 1NMS NFs. In contrast, annealing effectively reduces the defects of the material, so the mobility of $1NMS_{250-3h}$ NFs is the highest. We all know that the product of carrier concentration and mobility is proportional to the conductivity of the material, and conductivity is a parameter that describes the movement of carriers in substance [45]. Through calculating the conductivity of three substrate materials, the conductivity of $1NMS_{250-3h}$ NFs is 2 orders of magnitude higher than that of 1NMS NFs and 3 orders of magnitude higher than that of MoS_2 NFs. This indicates a higher efficiency charge transfer occurred between $1NMS_{250-3h}$ NFs and molecules. The LSV and EIS results also support this conclusion. As shown in Fig. 5(e), under the same conditions, $1NMS_{250-3h}$ NFs has a larger current density, and the Tafel slope is 79 mV/decade (Figure S12), which is much lower than pure MoS_2 and 1NMS NFs. The EIS results indicated that $1NMS_{250-3h}$ NFs have a smaller charge transfer resistance (Fig. 5(f)). The above
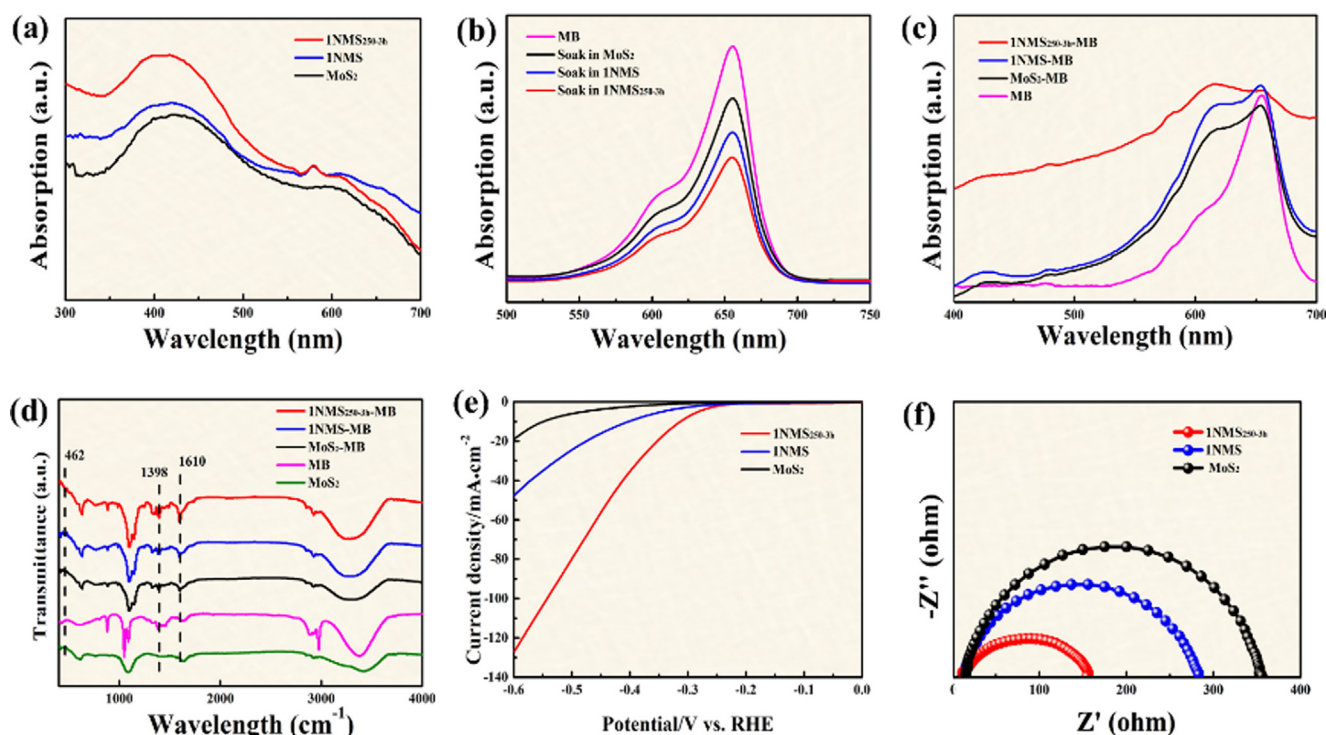

Fig. 5. (a) UV–vis spectra of MoS_2, 1NMS and $1NMS_{250-3h}$ NFs. (b) UV–vis spectra of pristine MB solution and supernatant solution after soaking with MoS_2, 1NMS and $1NMS_{250-3h}$ NFs, respectively. (c) UV–vis spectra of MoS_2, 1NMS and $1NMS_{250-3h}$ NFs after MB adsorption. (d) FTIR spectra of MoS_2, 1NMS and $1NMS_{250-3h}$ NFs after MB adsorption. (e) LSV curves of MoS_2, 1NMS and $1NMS_{250-3h}$ NFs. (f) Nyquist plots of MoS_2, 1NMS and $1NMS_{250-3h}$ NFs.

analysis shows that 1NMS$_{250-3h}$ NFs have higher carrier concentration and excellent carrier transport ability, which are the main factors for the high SERS sensitivity of 1NMS$_{250-3h}$ NFs.

The interface interaction and charge transfer effects between MB and MoS$_2$, 1NMS and 1NMS$_{250-3h}$ NFs were further studied by DFT calculation. Considering the complexity and computational cost of the research system, we adopt an optimized simple model is used here. Fig. 6(a)-(c) show the top view and side view of the MB molecular model structure adsorbing on MoS$_2$, 1NMS and 1NMS$_{250-3h}$, respectively. In this configuration, the adsorption energies of MB molecules on these substrates are −1.41 eV (MoS$_2$), −2.41 eV (1NMS) and −4.11 eV(1NMS$_{250-3h}$), respectively. Thus, the interaction between MB molecule and 1NMS$_{250-3h}$ NFs is the strongest. Bader charge analysis studies the interface charge transfer between different substrates and MB molecules:

$$\Delta\rho = \rho_{MB\text{-}substrate} - \rho_{MB} - \rho_{substrate}$$

Where $\rho_{MB\text{-}substrate}$, ρ_{MB}, $\rho_{substrate}$ are the charge densities of the MB-substrate system, MB, and substrate, respectively. And the calculation results are shown in Fig. 6(d)-(f), the charge transfer amount in the 1NMS$_{250-3h}$ NFs and MB system is 0.947 e/molecule, which is much larger than that of MoS$_2$ NFs (0.060 e/molecule). The high amount of charge transfer effectively increases the polarization tensor of the molecule, resulting in higher Raman scattering intensity [46]. At the same time, the charge transfer also allows more electrons to participate in the Raman scattering process, which enhances the electron–phonon coupling [47]. In addition, in the 1NMS$_{250-3h}$ NFs and MB system, the electrons and holes generated by the interface charge transfer are distributed on the surface of substrate and the surface of MB, respectively (yellow and cyan indicate the electron accumulation and depletion regions), and form an obvious dipole. The existence of dipole is conducive to enhance the Raman signal of MB [48]. According to Fermi's Golden Law, the probability of electronic transition in the charge transfer process is related to the density of states near the substrate Fermi level [49]. In Fig. 6(g)-(i), the 1NMS$_{250-3h}$ NFs have more electronic states near the Fermi level, and there is a stronger orbital interaction with MB. This increases the probability of the electronic transition between substrates and molecules, thus the substrate has a better Raman enhancement effect [50]. The above theoretical calculation results are in good agreement with our experimental results, charge transfer effect and interaction between substrates and molecules are improved by doping and annealing engineering, which are beneficial for the observed Raman signal enhancement.

Furthermore, we have analyzed a series of band structure include 1NMS$_{250-3h}$ NFs and MB. First, the valence band structure of 1NMS$_{250-3h}$ NFs was determined by XPS analysis (Figure S13).
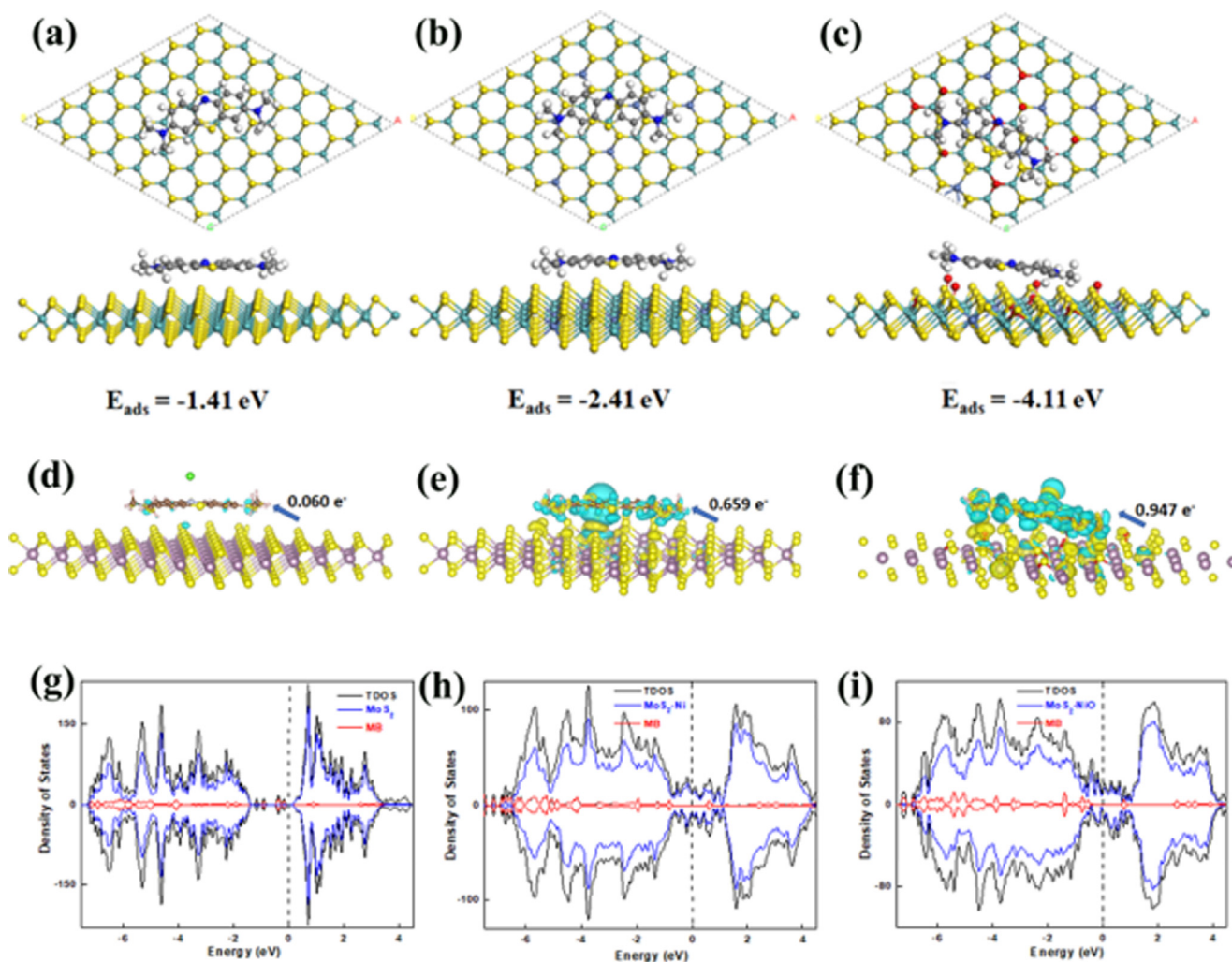

Fig. 6. Density functional theory (DFT) calculation results of MB adsorption on MoS$_2$ NFs, 1NMS NFs and 1NMS$_{250-3h}$ NFs. Top and side views of MB molecules adsorbed on the (a)MoS$_2$ NFs, (b)1NMS NFs and (c)1NMS$_{250-3h}$ NFs. Charge density difference of MB on the (d)MoS$_2$ NFs, (e)1NMS NFs and (f)1NMS$_{250-3h}$ NFs. Density of states for (g) "MB-MoS$_2$ NFs", (h) "MB-1NMS NFs" and (i) "MB-1NMS$_{250-3h}$ NFs".
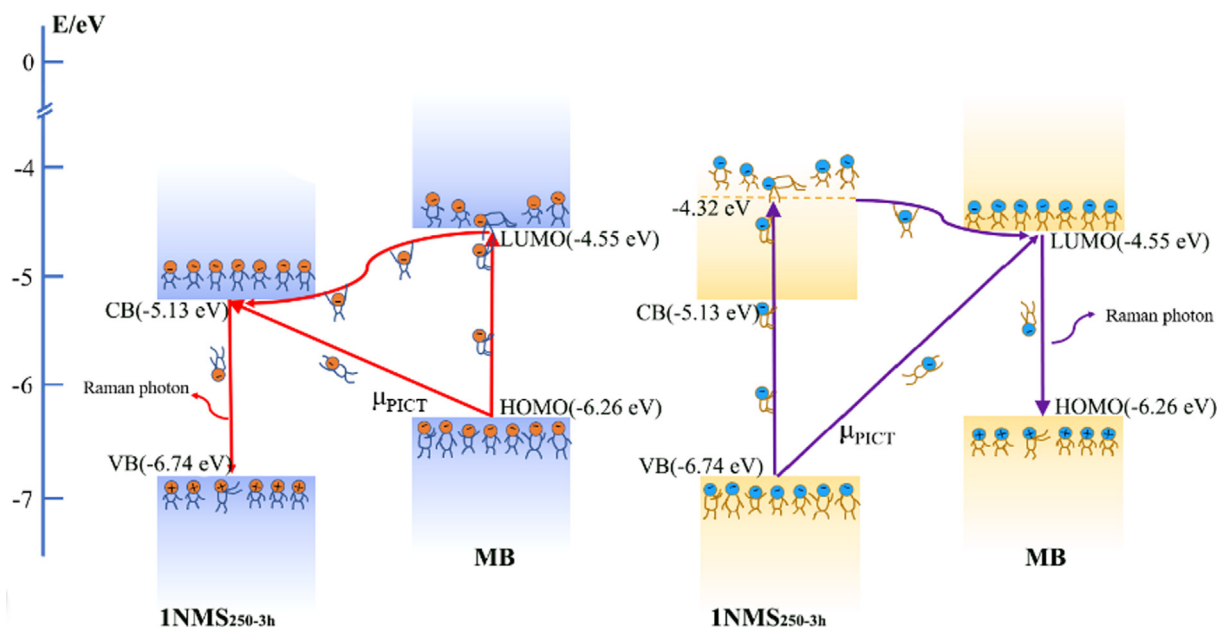
Fig. 7. Schematic energy diagram of charge transfer process between MB molecule and 1NMS$_{250-3h}$ NFs.
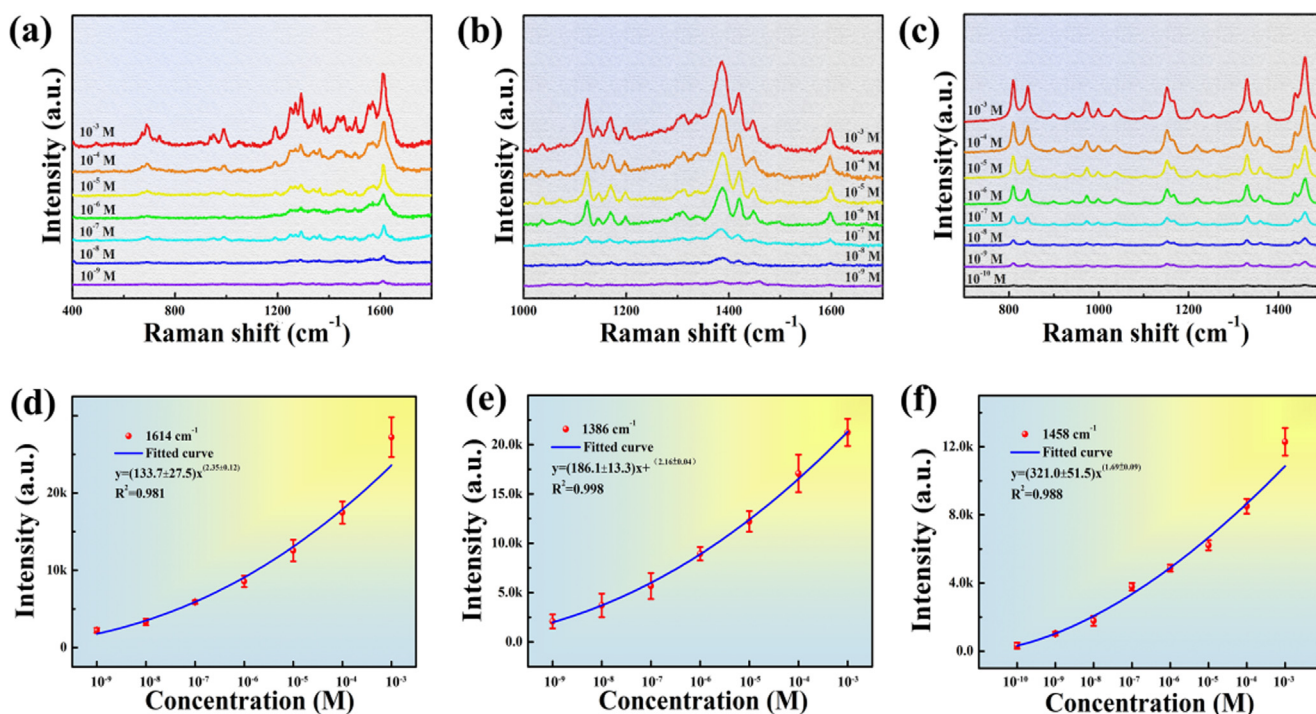

Fig. 8. SERS spectra recorded from 1NMS$_{250-3h}$ NFs substrate for (a) bilirubin, (b) BPA and (c) trichlorfon with different concentrations. (d) The diagram depicting concentration vs intensity plot of 1614 cm^{-1} of bilirubin. (e) The diagram depicting concentration vs intensity plot of 1386 cm^{-1} of BPA. (f) The diagram depicting concentration vs intensity plot of 1458 cm^{-1} of trichlorfon.

Relative to the Fermi level, the valence band structure of 1NMS$_{250-3h}$ NFs was 2.62 eV. In addition, electrochemical Mott-Schottky provides more electronic structure information for determining the Fermi level, and the flat band potential of 1NMS$_{250-3h}$ NFs is determined to be −0.588 eV (Figure S14(c)). The UV–vis spectrum analysis that the band gap of 1NMS$_{250-3h}$ NFs is 1.61 eV (Figure S15). Based on the above analysis, the energy level diagram of 1NMS$_{250-3h}$ NFs and MB is shown in Fig. 7. There are two possible charge transfer processes: (1) charge transfer from molecules to substrates, (2) charge transfer from substrates to molecules. In the first charge transfer process (blue part), the ground state electrons of MB undergo a photoinduced charge transfer (PICT) process from the highest occupied molecular orbital (HOMO) to the conduction band (CB) energy level of 1NMS$_{250-3h}$ NFs. At the same time, under the excitation of the 514 nm laser, the ground state electrons of MB transition from the HOMO energy level to the lowest unoccupied molecular orbital (LUMO) energy level. However, due to the chemical potential difference between MB and

1NMS$_{250-3h}$ NFs, the electrons of the LUMO energy level of MB are transferred to the CB of 1NMS$_{250-3h}$ NFs. Then the electrons recombine with the holes at the valence band (VB) energy level of 1NMS$_{250-3h}$ NFs, thereby releasing Raman photons. In the second charge transfer process (yellow part), the charge transfer transition energy (2.19 eV) from the VB energy level (−6.74 eV) of 1NMS$_{250-3h}$ NFs to the LUMO energy level (−4.55 eV) of MB better matches the excitation wavelength (2.41 eV), this may cause charge transfer resonance. Furthermore, the ground state electrons of 1NMS$_{250-3h}$ NFs are excited to a higher energy state (−4.32 eV) under the action of a laser with a wavelength of 514 nm. Electrons in this state transfer to the LUMO level of MB, then return to the HOMO level of MB and release Raman photons. These contributions enable 1NMS$_{250-3h}$ NFs to enhance the Raman signal of MB [13,43,51–53].

2.4. Application of 1NMS$_{250-3h}$ NFs in the detection of different types of pollutants

At present, there have been many related reports on electrochemical biosensors, which have realized the detection of substances such as biomolecules and food additives [54–57]. However, here we provide a quick detection method. Here biopigment (bilirubin), endocrine disruptors (bisphenol A) and organophosphorus pesticides (trichlorfon) were selected as analytes to evaluate the universality of SERS substrates.

Bilirubin is the main pigment in human bile, but it is toxic and has irreversible damage to the brain and nervous system. In addition, bilirubin is also a key basis for clinical judgment of jaundice and liver function. Therefore, 1NMS$_{250-3h}$ NFs was chosen as the substrate to detect bilirubin. The distribution of the main characteristic peak vibration modes of bilirubin is shown in Table S7 [58]. Fig. 8(a) and Figure S16(a)-(b) shows the changes in the Raman intensity of bilirubin at different concentrations on the 1NMS$_{250-3h}$ NFs substrate, and the minimum detection limit in serum can be as low as 10^{-9} M. We considered the strong peaks of bilirubin at 1614 cm^{-1} and estimated intensities (y) by fitting with Lorentzian functions. The value for each concentration (x) is the average intensity of the three spectra. Fig. 8(d) shows the concentration-dependent y. The intensity of the modes versus × follow the power law relationship (y=(133.7 ± 27.5)x$^{(2.3-5±0.12)}$). The R^2 value (0.981) for both the cases represents the goodness of the fitting.

As an important organic chemical raw material, BPA is widely used in the manufacturing process of food packaging. However, BPA has hormone-like properties and is an endocrine disruptor that has a negative impact on human health. Therefore, it is necessary to carry out a trace detection of BPA. The distribution of the vibration modes of the main characteristic peaks of BPA is shown in Table S8 [59], and the vibration mode at 1386 cm^{-1} is selected as the characteristic peak. As the concentration decreases, the intensity of the characteristic peak gradually decreases. When the concentration of BPA is as low as 10^{-9} M (Fig. 8(b) and Figure S16(c-d)), the existence of characteristic peaks can still be found. Its minimum detection limit can be as low as 10^{-9} M, which meets the actual detection limit. The relationship between the intensity of the Raman peak at 1386 cm^{-1} and the concentration is shown in Fig. 8(e). The result shows the excellent ability of quantitatively detecting BPA.

As a typical insecticide, trichlorfon is widely used in fruits, vegetables and other crops. However, trichlorfon residues on fruits and vegetables pose a serious threat to people's health. Therefore, a quick detection method is needed to detect it. We quickly detect it on the 1NMS$_{250-3h}$ NFs substrate through SERS means, according to Fig. 8(c) and Figure S16(e-f), the minimum detection limit is as low as 10^{-10} M. Table S9 shows its characteristic peak vibration mode [60]. The peak at 1458 cm^{-1} is selected for fitting. The result
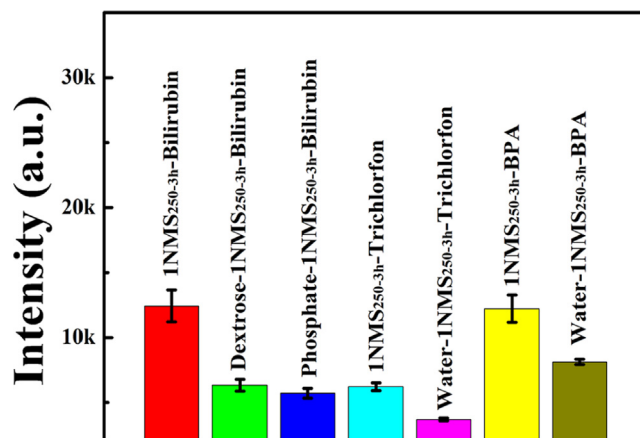

Fig. 9. Bar diagram depicting the Raman intensity of the 1614 cm^{-1} mode of bilirubin when the measurement was performed in 1NMS$_{250-3h}$ + bilirubin (red bar), 1NMS$_{250-3h}$ + dextrose + bilirubin (green bar), 1NMS$_{250-3h}$ + phosphate + bilirubin (blue bar). Bar diagram depicting the Raman intensity of the 1458 cm^{-1} mode of bilirubin when the measurement was performed in 1NMS$_{250-3h}$ + trichlorfon(cyan bar), 1NMS$_{250-3h}$ + water + trichlorfon (magenta bar). Bar diagram depicting the Raman intensity of the 1386 cm^{-1} mode of bilirubin when the measurement was performed in 1NMS$_{250-3h}$ + BPA(yellow), 1NMS$_{250-3h}$ + phosphate + BPA (dark yellow). The pollutants concentration was kept constant at 1 × 10^{-5} M for all the measurements.

is shown in Fig. 8(f), showing a good relationship, which can provide a basis for its quantitative analysis.

In order to further verify the anti-interference capability of the 1NMS$_{250-3h}$ NFs SERS substrate, Raman analysis was carried out by adding different interfering substances. As shown in Fig. 9 and Figure S17, although the Raman intensity is reduced, it can still clearly identify the characteristic peaks of pollutants in the presence of interference. Table S10-S12 shows the comparison of detection limits (bilirubin, BPA, and trichlorfon) on different substrates. The results showed that the prepared 1NMS$_{250-3h}$ NFs had highest sensitivity, which is very rare for non-noble metal materials. Therefore, these study demonstrated the excellent selectivity, reproducibility, and high-efficiency detection capability of 1NMS$_{250-3h}$ NFs.

3. Discussion

In summary, we successfully constructed more versatile and sensitive SERS substrates by treating MoS$_2$ NFs in two steps of doping and annealing. The enhancement mechanism of the optimized MoS$_2$ NFs was investigated by combining theoretical calculations and experiments. After doping, the carrier concentration and interaction with probe molecules of MoS$_2$ NFs increased. The annealing process enhances the conductivity of MoS$_2$ NFs and improves the carrier transport efficiency. Thus, the SERS sensitivity of MoS$_2$ NFs is improved, and the enhancement factor for MB can reach 7.74 × 10^6. More importantly, this strategy does not rely on the molecular resonance effect of probe molecules, and can detect other types of probe molecules with high sensitivity. We detected three different types of representative substances, bilirubin, cytochrome C and trichlorfon respectively, and finally achieved low-concentration detection. The results of this study provide a low-cost semiconductor SERS substrate and provide a reference for promoting the practical application of semiconductor SERS substrates.

CRediT authorship contribution statement

Rui Su: Writing – original draft. **Shuo Yang:** Data curation. **Donglai Han:** Software. **Mingyue Hu:** Visualization. **Yang Liu:**

Investigation. **Jinghai Yang:** Supervision. **Ming Gao:** Writing – review & editing.

Data availability

Data will be made available on request.

Declaration of Competing Interest

The authors declare that they have no known competing financial interests or personal relationships that could have appeared to influence the work reported in this paper.

Acknowledgements

Appendix A. Supplementary data

Supplementary data to this article can be found online at https://doi.org/10.1016/j.jcis.2022.12.075.

References

[1] I. Alessandri, J.R. Lombardi, Enhanced Raman Scattering with Dielectrics, Chem. Rev. 116 (2016) 14921–14981.

[2] S. Yang, J. Yao, Y. Quan, M. Hu, R. Su, M. Gao, D. Han, J. Yang, Monitoring the charge-transfer process in a Nd-doped semiconductor based on photoluminescence and SERS technology, Light Sci. Appl. 9 (2020) 117.

[3] J. Jin, W. Song, J. Wang, L. Li, Y. Tian, S. Zhu, Y. Zhang, S. Xu, B. Yang, B. Zhao, A highly sensitive SERS platform based on small-sized Ag/GQDs nanozyme for intracellular analysis, Chem. Eng. J. 430 (2022) 132687.

[4] G. Demirel, R.L.M. Gieseking, R. Osgood, S. Kahmann, M.A. Loi, G.C. Schatz, A. Facchetti, H. Usta, Molecular engineering of organic semiconductors enables noble metal-comparable SERS enhancement and sensitivity, Nat. Commun. 10 (2019) 5502.

[5] M. Caban-Acevedo, M.L. Stone, J.R. Schmidt, J.G. Thomas, Q. Ding, H.C. Chang, M.L. Tsai, J.H. He, S. Jin, Efficient hydrogen evolution catalysis using ternary pyrite-type cobalt phosphosulphide, Nat. Mater. 14 (2015) 1245–1251.

[6] Q. Lu, Y. Yu, Q. Ma, B. Chen, H. Zhang, 2D Transition-Metal-Dichalcogenide-Nanosheet-Based Composites for Photocatalytic and Electrocatalytic Hydrogen Evolution Reactions, Adv. Mater. 28 (2016) 1917–1933.

[7] L.B. Wang, H.Y. Tan, L.Y. Zhang, B. Cheng, J.G. Yu, In-situ growth of few-layer graphene on ZnO with intimate interfacial contact for enhanced photocatalytic CO₂ reduction activity, Chem. Eng. J. 411 (2021) 128501.

[8] G. Song, W. Gong, S. Cong, Z. Zhao, Ultrathin Two-Dimensional Nanostructures: Surface Defects for Morphology-Driven Enhanced Semiconductor SERS, Angew. Chem. Int. Ed. Engl. 60 (2021) 5505–5511.

[9] Z. Zheng, S. Cong, W. Gong, J. Xuan, G. Li, W. Lu, F. Geng, Z. Zhao, Semiconductor SERS enhancement enabled by oxygen incorporation, Nat. Commun. 8 (2017) 1993.

[10] J. Zhang, C. Qin, Y. Zhong, X. Wang, W. Wang, D. Hu, X. Liu, C. Xue, R. Zhou, L. Shen, Y. Song, D. Xu, Z. Lin, J. Guo, H. Su, D.-S. Li, T. Wu, Atomically precise metal-chalcogenide semiconductor molecular nanoclusters with high dispersibility: Designed synthesis and intracluster photocarrier dynamics, Nano Res. 13 (2020) 2828–2836.

[11] Y. Feng, K.E. Marusak, L. You, S. Zauscher, Biosynthetic transition metal chalcogenide semiconductor nanoparticles: Progress in synthesis, property control and applications, Curr. Opin. Colloid In. 38 (2018) 190–203.

[12] H. Li, X. Wang, X. Zhu, X. Duan, A. Pan, Composition modulation in one-dimensional and two-dimensional chalcogenide semiconductor nanostructures, Chem. Soc. Rev. 47 (2018) 7504–7521.

[13] Y. Quan, R. Su, S. Yang, L. Chen, M. Wei, H. Liu, J. Yang, M. Gao, B. Li, In-situ surface-enhanced Raman scattering based on MTi₂₀ nanoflowers: Monitoring and degradation of contaminants, J. Hazard. Mater. 412 (2021) 125209.

[14] P. Karthick Kannan, P. Shankar, C. Blackman, C.H. Chung, Recent Advances in 2D Inorganic Nanomaterials for SERS Sensing, Adv. Mater. 31 (2019) e1803432.

[15] A. Sebastian, R. Pendurthi, T.H. Choudhury, J.M. Redwing, S. Das, Benchmarking monolayer MoS₂ and WS₂ field-effect transistors, Nat. Commun. 12 (2021) 693.

[16] A.R. Brill, A. Kafri, P.K. Mohapatra, A. Ismach, G. de Ruiter, E. Koren, Modulating the Optoelectronic Properties of MoS₂ by Highly Oriented Dipole-Generating Monolayers, ACS Appl. Mater. Inter. 13 (2021) 32590–32597.

[17] C.S. K, R.C. Longo, R. Addou, R.M. Wallace, K. Cho, Impact of intrinsic atomic defects on the electronic structure of MoS₂ monolayers, Nanotechnology. 25 (2014) 375703.

[18] S. Chen, Y. Pan, Influence of Group III and IV Elements on the Hydrogen Evolution Reaction of MoS₂ Disulfide, J. Phys. Chem. C. 125 (2021) 11848–11856.

[19] X. Qiu, T. Zhang, Z. Dai, R. Cao, T. Wei, Effect of one-step hydrothermal reaction conditions on the crystal growth of nano-/micro-MoS₂, Ionics. 28 (2022) 939–949.

[20] M. Gao, J. Yao, J. Li, R. Su, Y. Liu, L. Chen, J. Yang, A Novel Strategy for Improving SERS Activity by Cerium Ion f→d Transitions for Rapid Detection of Endocrine Disruptor, Chem. Eng. J. 403 (2021) 131467.

[21] A. Fularz, S. Almohammed, J.H. Rice, Oxygen Incorporation-Induced SERS Enhancement in Silver Nanoparticle-Decorated ZnO Nanowires, ACS Appl. Nano Mater. 3 (2020) 1666–1673.

[22] C.J. Boyle, M. Upadhyaya, P. Wang, L.A. Renna, M. Lu-Diaz, S. Pyo Jeong, N. Hight-Huf, L. Korugic-Karasz, M.D. Barnes, Z. Aksamija, D. Venkataraman, Tuning charge transport dynamics via clustering of doping in organic semiconductor thin films, Nat. Commun. 10 (2019) 2827.

[23] C. Hu, L. Dai, Doping of Carbon Materials for Metal-Free Electrocatalysis, Adv. Mater. 31 (2019) e1804672.

[24] M. Wood, J.J. Kuo, K. Imasato, G.J. Snyder, Improvement of Low-Temperature zT in a Mg₃Sb₂ -Mg₃Bi₂ Solid Solution via Mg-Vapor Annealing, Adv. Mater. 31 (2019) e1902337.

[25] Y. Liu, P. Stradins, S.H. Wei, Air Passivation of Chalcogen Vacancies in Two-Dimensional Semiconductors, Angew. Chem. Int. Ed. Engl. 55 (2016) 965–968.

[26] R. Su, Y. Quan, S. Yang, M. Hu, J. Yang, M. Gao, Destroying the symmetric structure to promote phase transition: Improving the SERS performance and catalytic activity of MoS₂ nanoflowers, J. Alloy. Compd. 886 (2021) 161268.

[27] M. Hu, Y. Quan, S. Yang, R. Su, H. Liu, M. Gao, L. Chen, J. Yang, Self-cleaning semiconductor heterojunction substrate: ultrasensitive detection and photocatalytic degradation of organic pollutants for environmental remediation, Microsyst. Nanoeng. 6 (2020) 111.

[28] S. Wang, D. Zhang, B. Li, C. Zhang, Z. Du, H. Yin, X. Bi, S. Yang, Ultrastable In-Plane 1T–2H MoS₂ Heterostructures for Enhanced Hydrogen Evolution Reaction, Adv. Energy Mater. 8 (2018) 1801345.

[29] J. Chen, Y. Liao, X. Wan, S. Tie, B. Zhang, S. Lan, X. Gao, A high performance MoO₃@MoS₂ porous nanorods for adsorption and photodegradation of dye, J. Solid State Chem. 291 (2020) 121652.

[30] L. Wang, X. Ji, T. Wang, Q. Zhang, Novel Red Emission from MoO₃/MoS₂-MoO₂-MoO₃ Core-Shell Belt Surface, ACS Appl. Mater. Inter. 10 (2018) 36297–36303.

[31] M. Wen, X. Chen, Z. Zheng, S. Deng, Z. Li, W. Wang, H. Chen, In-Plane Anisotropic Raman Spectroscopy of van der Waals α-MoO₃, J. Phys. Chem. C. 125 (2020) 765–773.

[32] M. Yilmaz, M. Ozdemir, H. Erdogan, U. Tamer, U. Sen, A. Facchetti, H. Usta, G. Demirel, Micro-/Nanostructured Highly Crystalline Organic Semiconductor Films for Surface-Enhanced Raman Spectroscopy Applications, Adv. Funct. Mater. 25 (2015) 5669–5676.

[33] H. Park, N. Liu, B.H. Kim, S.H. Kwon, S. Baek, S. Kim, H.K. Lee, Y.J. Yoon, S. Kim, Exceptionally Uniform and Scalable Multilayer MoS₂ Phototransistor Array Based on Large-Scale MoS₂ Grown by RF Sputtering, Electron Beam Irradiation, and Sulfurization, ACS Appl. Mater. Inter. 12 (2020) 20645–20652.

[34] Y. Xu, J. Qu, Y. Li, M. Zhu, Y. Liu, R. Zheng, J.M. Cairney, W. Li, Bridging metal-ion induced vertical growth of MoS₂ and overall fast electron transfer in (C, P)₃N-4-M (Ni²⁺, Co²⁺)-Mo₂ electrocatalyst for efficient hydrogen evolution reaction, Sustain. Mater. Technol. 25 (2020) e00172.

[35] S. Duraisamy, A. Ganguly, P.K. Sharma, J. Benson, J. Davis, P. Papakonstantinou, One-Step Hydrothermal Synthesis of Phase-Engineered MoS₂/MoO₃ Electrocatalysts for Hydrogen Evolution Reaction, ACS Appl. Nano Mater. 4 (2021) 2642–2656.

[36] J. Seo, J. Lee, Y. Kim, D. Koo, G. Lee, H. Park, Ultrasensitive Plasmon-Free Surface-Enhanced Raman Spectroscopy with Femtomolar Detection Limit from 2D van der Waals Heterostructure, Nano Lett. 20 (2020) 1620–1630.

[37] P. Cai, J. Chen, Y. Ding, Y. Liu, Z. Wen, Defect-Rich MoO₃ Nanobelt Cathode for a High-Performance Hybrid Alkali/Acid Zn-MoO₃ Rechargeable Battery, ACS Sustain. Chem. Eng. 9 (2021) 11524–11533.

[38] S.K. Gahlaut, P. Devi, J.P. Singh, Self-sustainable and recyclable Ag nanorods for developing Ag-Ag₂S nano heterostructures using sewage gas: Applications in photocatalytic water purification, hydrogen evolution SERS and antibacterial activity, Appl. Surf. Sci. 528 (2020) 147037.

[39] M. Haroon, I. Abdulazeez, T.A. Saleh, A.A. Al-Saadi, Electrochemically modulated SERS detection of procaine using FTO electrodes modified with silver-decorated carbon nanosphere, Electrochim. Acta. 387 (2021) 138463.

[40] Y. Ye, W. Yi, W. Liu, Y. Zhou, H. Bai, J. Li, G. Xi, Remarkable surface-enhanced Raman scattering of highly crystalline monolayer Ti₃C₂ nanosheets, Sci. China Mater. 63 (2020) 794–805.

[41] L. Yang, J. Hu, L. He, J. Tang, Y. Zhou, J. Li, K. Ding, One-pot synthesis of multifunctional magnetic N-doped graphene composite for SERS detection, adsorption separation and photocatalytic degradation of Rhodamine 6G, Chem. Eng. J. 327 (2017) 694–704.

[42] R. Chen, L. Zhang, X. Li, L. Ong, Y.G. Soe, N. Sinsua, S.L. Gras, R.F. Tabor, X. Wang, W. Shen, Trace Analysis and Chemical Identification on Cellulose Nanofibers-Textured SERS Substrates Using the "Coffee Ring" Effect, ACS Sensors. 2 (2017) 1060–1067.

[43] J.R. Lombardi, R.L. Birke, Theory of Surface-Enhanced Raman Scattering in Semiconductors, J. Phy. Chem. C. 118 (2014) 11120–11130.

[44] A. Saha, R. Kurrey, M.K. Deb, S.K. Verma, Resin immobilized gold nanocomposites assisted surface enhanced infrared absorption (SEIRA) spectroscopy for improved surface assimilation of methylene blue from aqueous solution, Spectrochim. Acta A Mol. Biomol. Spectrosc. 262 (2021) 120144.

[45] X.Y. Zhang, S. Yang, L. Yang, D. Zhang, Y. Sun, Z. Pang, J. Yang, L. Chen, Carrier dynamic monitoring of a pi-conjugated polymer: a surface-enhanced Raman scattering method, Chem. Commun. 56 (2020) 2779–2782.

[46] X. Zheng, F. Ren, S. Zhang, X. Zhang, H. Wu, X. Zhang, Z. Xing, W. Qin, Y. Liu, C. Jiang, A General Method for Large-Scale Fabrication of Semiconducting Oxides with High SERS Sensitivity, ACS Appl. Mater. Inter. 9 (2017) 14534–14544.

[47] S. Zhao, H. Wang, L. Niu, W. Xiong, Y. Chen, M. Zeng, S. Yuan, L. Fu, 2D GaN for Highly Reproducible Surface Enhanced Raman Scattering, Small. 17 (2021) e2103442.

[48] H. Qiu, M. Wang, L. Zhang, M. Cao, Y. Ji, S. Kou, J. Dou, X. Sun, Z. Yang, Wrinkled 2H-phase MoS$_2$ sheet decorated with graphene-microflowers for ultrasensitive molecular sensing by plasmon-free SERS enhancement, Sensor Actuat. B-Chem. 320 (2020) 128445.

[49] X. Ling, W. Fang, Y.H. Lee, P.T. Araujo, X. Zhang, J.F. Rodriguez-Nieva, Y. Lin, J. Zhang, J. Kong, M.S. Dresselhaus, Raman enhancement effect on two-dimensional layered materials: graphene, h-BN and MoS$_2$, Nano Lett. 14 (2014) 3033–3040.

[50] Y. Song, H.C. Huang, W. Lu, N. Li, J. Su, S.B. Cheng, Y. Lai, J. Chen, J. Zhan, Ag@WS$_2$ quantum dots for Surface Enhanced Raman Spectroscopy: Enhanced charge transfer induced highly sensitive detection of thiram from honey and beverages, Food Chem. 344 (2021) 128570.

[51] P. Zuo, L. Jiang, X. Li, P. Ran, B. Li, A. Song, M. Tian, T. Ma, B. Guo, L. Qu, Y. Lu, Enhancing charge transfer with foreign molecules through femtosecond laser induced MoS$_2$ defect sites for photoluminescence control and SERS enhancement, Nanoscale. 11 (2019) 485–494.

[52] L. Zhao, C. Deng, S. Xue, H. Liu, L. Hao, M. Zhu, Multifunctional g-C3N4/Ag NPs intercalated GO composite membrane for SERS detection and photocatalytic degradation of paraoxon-ethyl, Chem. Eng. J. 402 (2020) 126223.

[53] X. Hou, Q. Lin, Y. Wei, Q. Hao, Z. Ni, T. Qiu, Surface-Enhanced Raman Scattering Monitoring of Oxidation States in Defect-Engineered Two-Dimensional Transition Metal Dichalcogenides, J. Phys. Chem. Lett. 11 (2020) 7981–7987.

[54] J. Wang, B.B. Yang, H.W. Wang, P. Yang, Y.K. Du, Highly sensitive electrochemical determination of Sunset Yellow based on gold nanoparticles/graphene electrode, Analytica Chimica Acta 893 (2015) 41–48.

[55] B.B. Yang, J. Wang, D. Bin, M.S. Zhu, P. Yang, Y.K. Du, A three dimensional Pt nanodendrite/graphene/MnO2 nanoflower modified electrode for the sensitive and selective detection of dopamine, J. Mater. Chem. B 3 (2015) 7440–7448.

[56] C.E. Zou, J.T. Zhong, S. Li, H.W. Wang, J. Wang, B. Yan, Y.K. Du, Fabrication of reduced graphene oxide-bimetallic PdAu nanocomposites for the electrochemical determination of ascorbic acid, dopamine, uric acid and rutin, J. Electroanal. Chem. 805 (2017) 110–119.

[57] H.Y. Shang, H. Xu, Q.Y. Liu, Y.K. Du, PdCu alloy nanosheets-constructed 3D flowers: New highly sensitive materials for H2S detection, Sensors Actuators B-Chem. 289 (2019) 260–268.

[58] S.S. Singha, S. Mondal, T.S. Bhattacharya, L. Das, K. Sen, B. Satpati, K. Das, A. Singha, Au nanoparticles functionalized 3D-MoS$_2$ nanoflower: An efficient SERS matrix for biomolecule sensing, Biosens. Bioelectron. 119 (2018) 10–17.

[59] P.-Y. Lin, C.-W. Hsieh, S. Hsieh, Rapid and Sensitive SERS Detection of Bisphenol A Using Self-assembled Graphitic Substrates, Sci. Rep. 7 (2017) 16698.

[60] C. Costa, R.A. Ando, A.C. Sant'Ana, P. Corio, Surface-enhanced Raman spectroscopy studies of organophosphorous model molecules and pesticides, Phys. Chem. Chem. Phys. 14 (2012) 15645–15651.